Supplemental Information for Manuscript “KY216-tubulin complex captures VASH2 to inhibit NSCLC metastasis”

Supplemental Figures

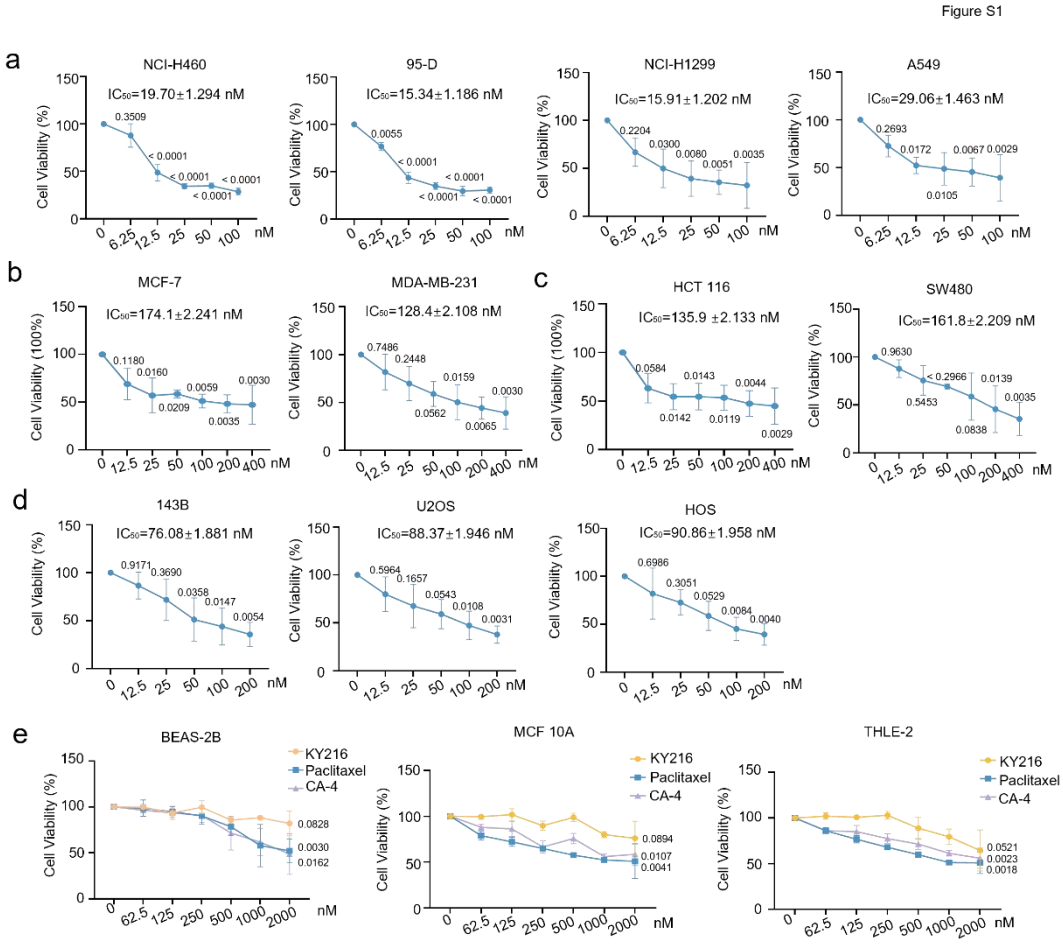

Supplementary Fig. 1. **KY216 demonstrated lower toxicity and higher selectivity in NSCLC cell lines compared to the microtubule-targeting drug paclitaxel CA-4.** **a** CCK-8 detected the cell viability of NCI-H460 (independant biological replicates n = 6), 95-D (independant biological replicates n = 6), H1299 (independant biological replicates n = 3) and A549 (independant biological replicates n = 3) cells induced by KY216. **b** CCK-8 detected the cell viability of MCF-7 and MDA-MB-231 cells induced by KY216 (independant biological replicates n = 3). **c** CCK-8 detected the cell viability of HCT-116 and SW480 cells induced by KY216 (independant biological replicates n = 3). **d** CCK-8 detected the cell viability of 143B, U2OS and HOS cells induced by KY216 (independant biological replicates n = 3). **e** CCK-8 detected the cell viability of BEAS-2B, MCF-10A, THLE-2 cells induced by KY216, paclitaxel, CA-4 (independant biological replicates n = 3). All data are shown as

means ± SEM. Values shown are *P* values and were calculated using the two-tailed Student's *t* tests (**e**) and one-way ANOVA with Tukey's comparisons test (**a-d**) in GraphPad Prism 9.5.0. All data marked with significance were compared to the 0 nM group. Source data are provided as a Source Data file.

Figure S2

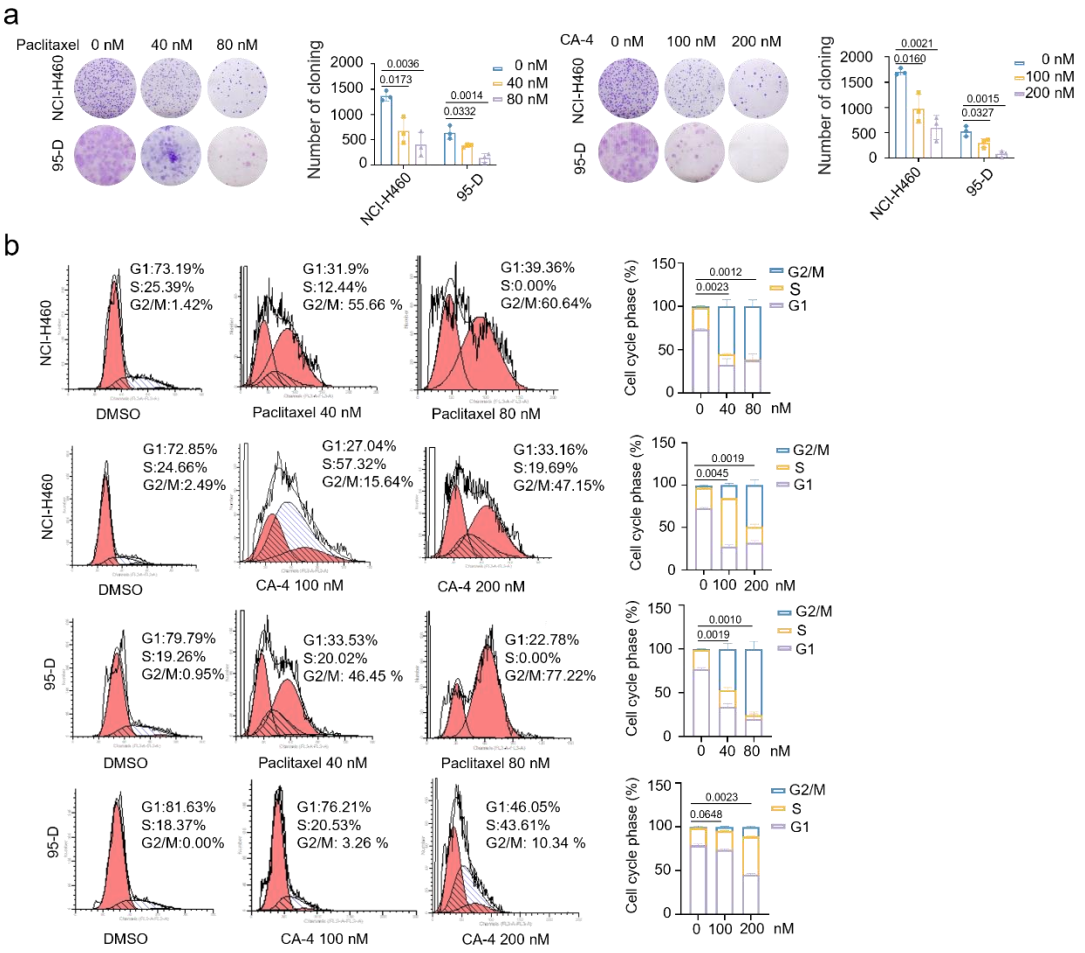

Supplementary Fig. 2. **The pharmacological effects of paclitaxel and CA-4 in NCI-H460 and 95-D cells. a** Effects of different concentrations of paclitaxel and CA-4 on the colony forming ability of NSCLC cells (independant biological replicates n = 3). **b** Effects of different concentrations of KY216, paclitaxel, and CA-4 on cell cycle blockade in NSCLC (independant biological replicates n = 3), with significance indicated by comparison of the G2/M phase proportion in each group. All data are shown as means ± SEM. Values shown are *P* values and were calculated using the two-tailed Student's *t* tests (**b**) and one-way ANOVA with Tukey's

comparisons test (**a**) in GraphPad Prism 9.5.0. Source data are provided as a Source Data file.

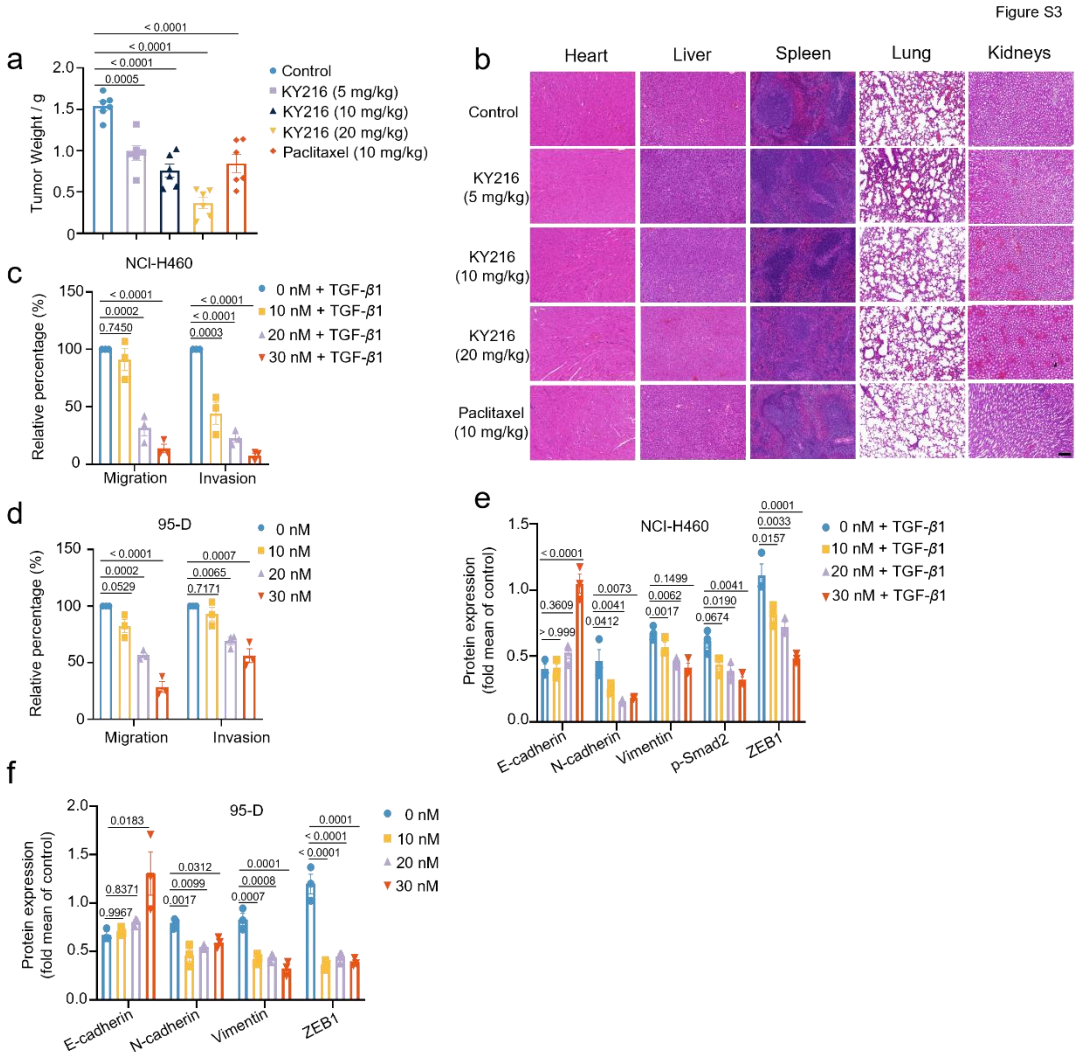

Supplementary Fig. 3. **KY216 significantly inhibited NSCLC migratory invasion and was superior to paclitaxel and CA-4.** **a** Tumor weight of nude mice with KY216 or paclitaxel treatment (n = 6 mice per group). **b** Representative H&E-stained images of mouse heart, liver, spleen, lung and kidney (n = 6 mice per group). Scale bar: 50 μm. **c, d** Quantitative data on the ability of KY216 to reduce migration and invasion of TGF-*β*-induced NCI-H460 and 95-D cells (independant biological replicates n = 3). **e, f** Quantitative protein blotting data demonstrating the effect of KY216 on migration and invasion of TGF-*β*-induced H460 and 95-D cells involving epithelial/mesenchymal markers, ZEB1 and p-Smad2 (independant biological

replicates n = 3). All data are shown as means ± SEM. Values shown are *P* values and were calculated using the one-way ANOVA with Tukey's comparisons test in GraphPad Prism 9.5.0. Source data are provided as a Source Data file.

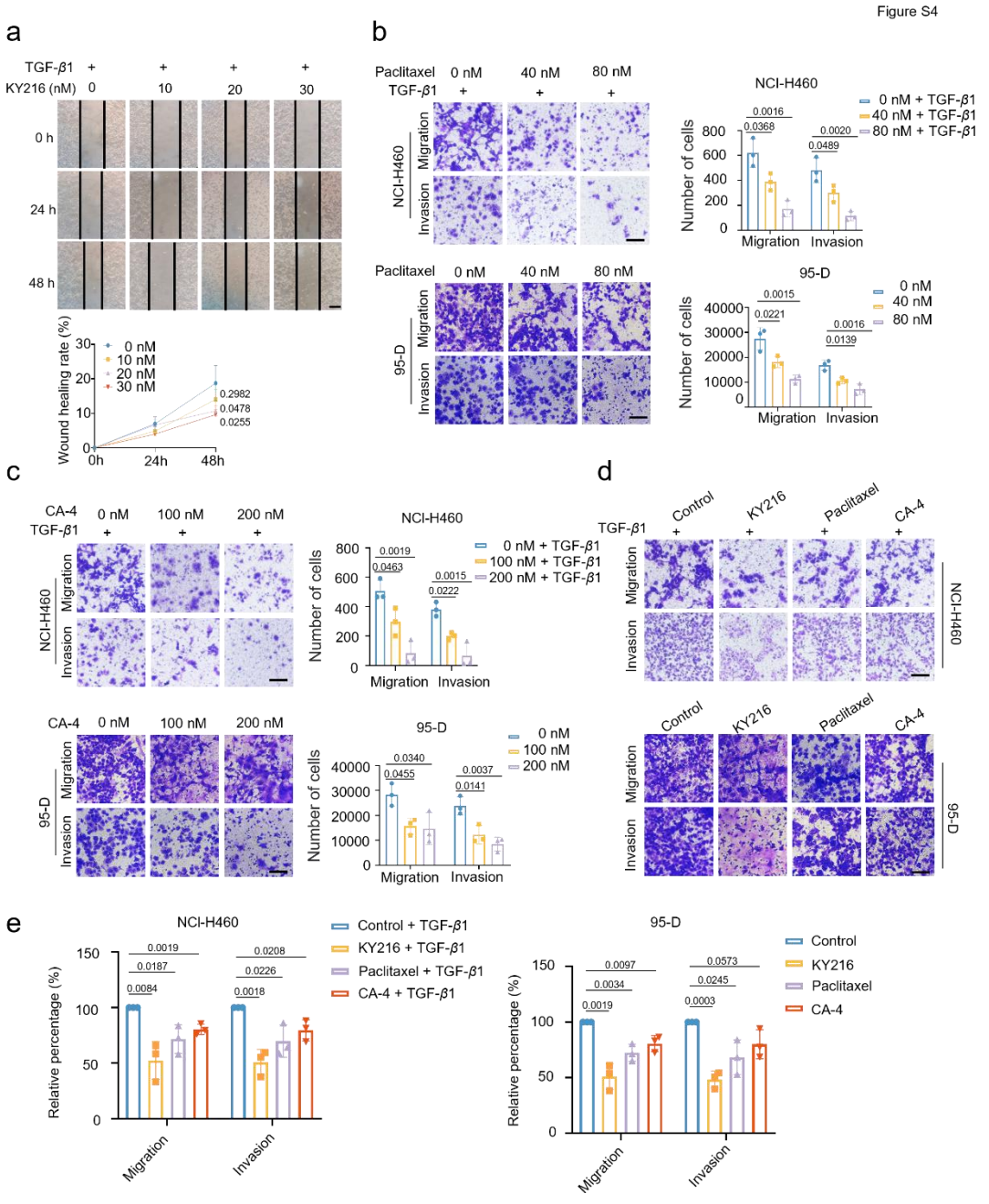

Supplementary Fig. 4. **Compared with paclitaxel and CA-4, KY216 exhibited a stronger inhibitory effect on the migration and invasion of non-small cell lung cancer cells.** **a** NCI-H460 cells subjected to scratch assay were treated with KY216

for 24 or 48 hours (independant biological replicates n = 3). Scale bar: 100 μm. **b, c** Effects of varying concentrations of paclitaxel and CA-4 on the migratory and invasive abilities of TGF-β-induced H460 and 95-D cells (independant biological replicates n = 3). Scale bar: 50 μm. **d, e** Inhibitory effects and relative quantification of 20 nM KY216, paclitaxel, and CA-4 on the migration and invasion of NCI-H460 and 95-D cells (independant biological replicates n = 3). Scale bar: 50 μm. Values shown are *P* values and were calculated using the two-tailed Student's *t* tests (**e**) and one-way ANOVA with Tukey's comparisons test (**b, c**) in GraphPad Prism 9.5.0. Source data are provided as a Source Data file.

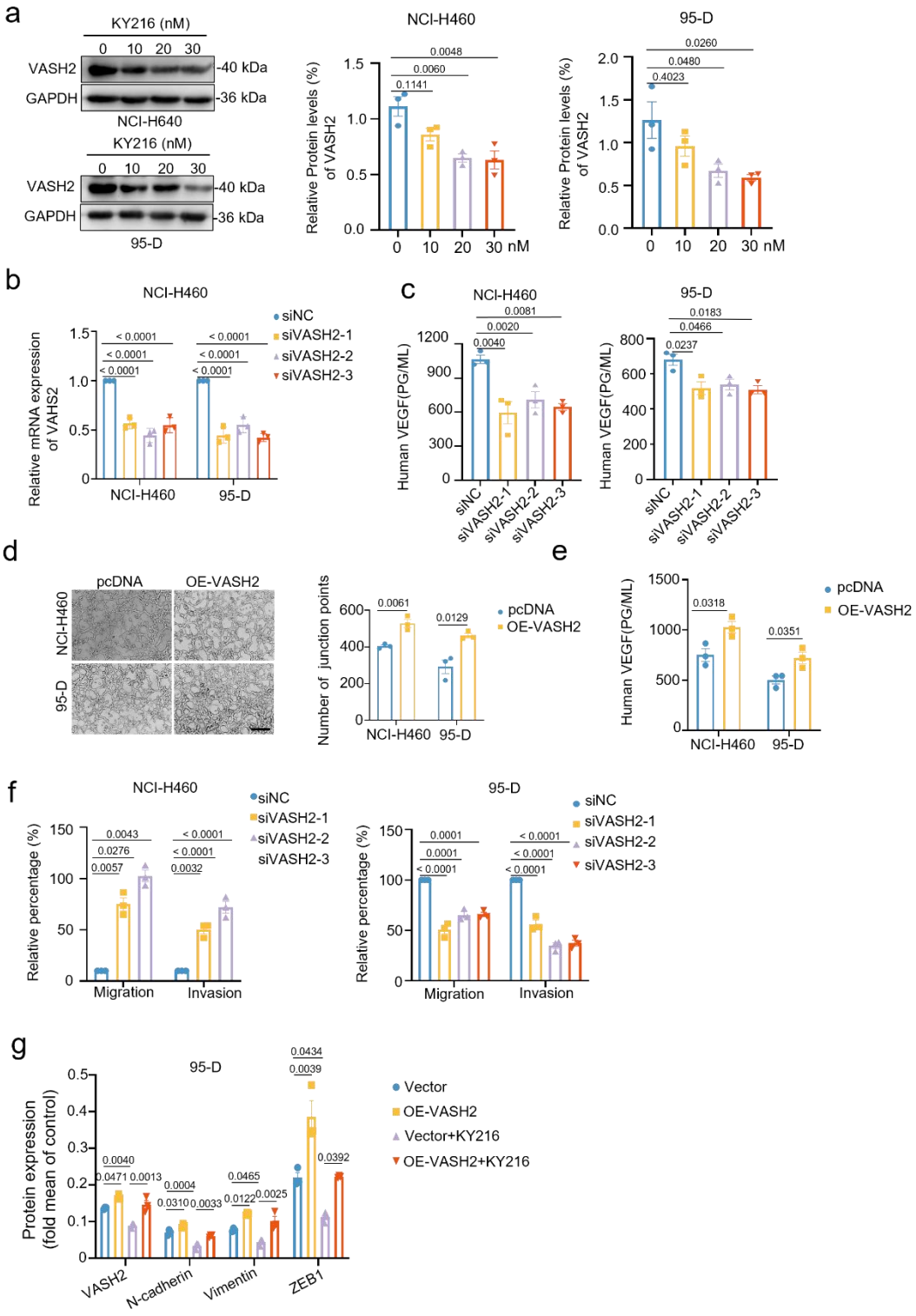

Supplementary Fig. 5. **VASH2 promotes NSCLC metastasis. a** VASH2 protein blot analysis in 1.5 million NCI-H460 and 95-D cells and the relative quantification of VASH2 protein expression following KY216 treatment (independant biological replicates n = 3). **b** Validation of knockdown efficiency of three siRNAs targeting

VASH2 in 7 × 10^5 95-D and NCI-H460 cells was performed using qRT-PCR (independant biological replicates n = 3). **c** Determination of VEGF expression levels in supernatants of NCI-H460 and 95-D cells transfected with siVASH2 (independant biological replicates n = 3). **d** Conditioned medium from NCI-H460 and 95-D cells transfected with OE-VASH2 plasmids promoted the formation of capillary-like tubular networks in HUVEC. Representative images are shown (independant biological replicates n = 3). Scale bar: 50 μm. **e** Determination of VEGF expression levels in supernatants of NCI-H460 and 95-D cells transfected with OE-VASH2 plasmids (independant biological replicates n = 3). **f** Quantitative data shows that transfected siVASH2 can reduce the migration and invasion of TGF-β-induced NCI-H460 and 95-D cells (independant biological replicates n = 3). **g** Quantitative data demonstrating that overexpression of VASH2 counteracts the inhibitory effect of KY216 on mesenchymal proteins and ZEB1 (independant biological replicates n = 3). All data are shown as means ± SEM. Values shown are *P* values and were calculated using the two-tailed Student's *t* tests (**d, e**) and one-way ANOVA with Tukey's comparisons test (**a-c, f, g**) in GraphPad Prism 9.5.0. Source data are provided as a Source Data file.

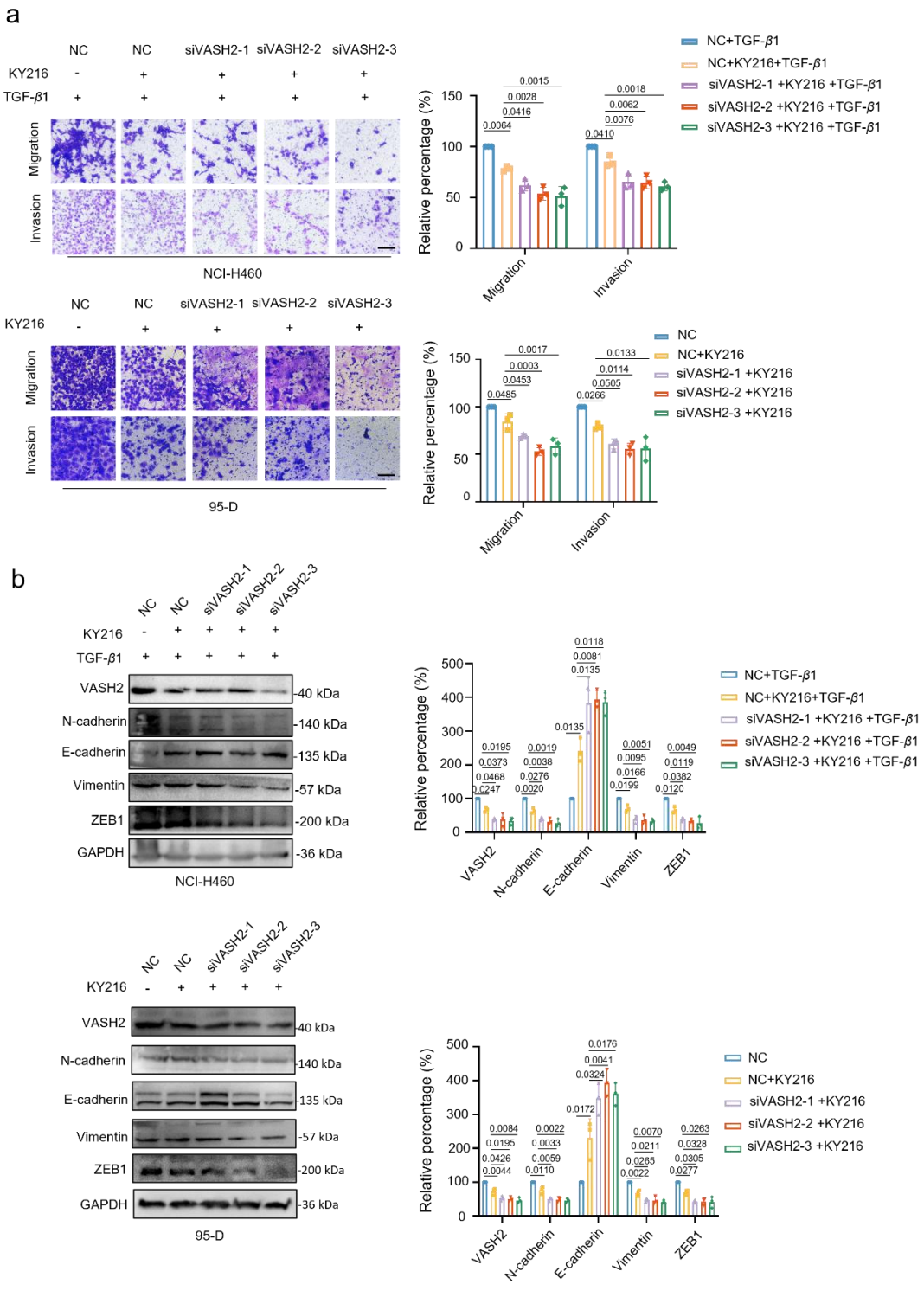

Supplementary Fig. 6. **Knockdown of VASH2 significantly potentiates the inhibitory effects of KY216 on TGF-*β*-induced migration and invasion in NCI-H460 cells and 95-D cells.** **a** Representative image of trans-well assay of NCI-H460 and 95-D cells treated with different treatments and their quantitatively

analyzed cell migration numbers are shown (independant biological replicates n = 3). Scale bar: 50 μm. **b** Representative Western blot analysis and corresponding quantitative analysis of epithelial and mesenchymal markers, as well as ZEB1 protein expression, are shown (independant biological replicates n = 3). All data are shown as means ± SEM. Values shown are *P* values and were calculated using the one-way ANOVA with Tukey's comparisons test in GraphPad Prism 9.5.0. Source data are provided as a Source Data file.

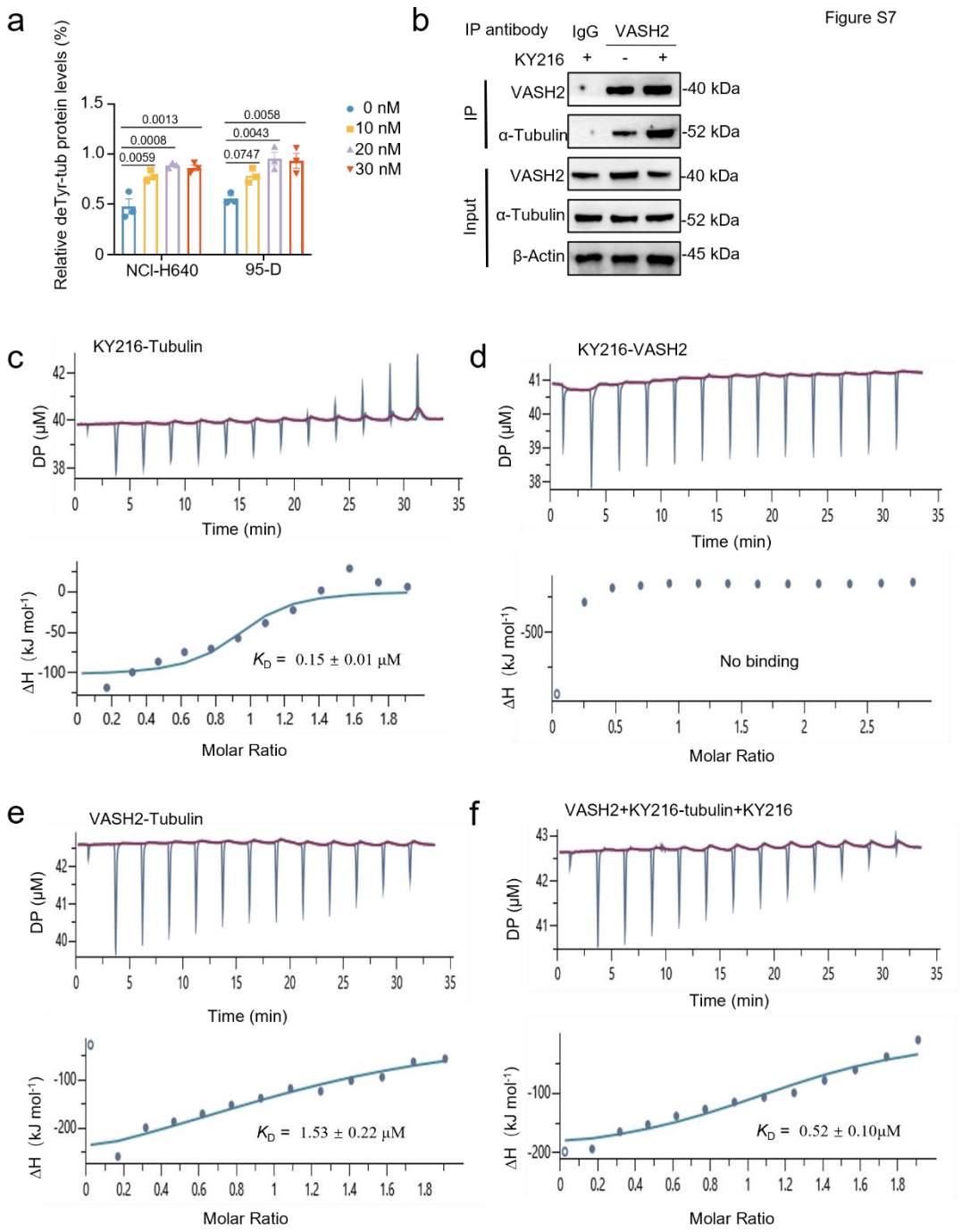

Supplementary Fig. 7. **The thermodynamic fundamentals of KY216 has been demonstrated to facilitate the interaction between VASH2 and α-tubulin.** **a** Quantitative data on the increase in the level of α-tubulin detyrosination induced by KY216 (independant biological replicates n = 3). All data are shown as means ± SEM. Values shown are *P* values and were calculated using the one-way ANOVA with Tukey's comparisons test in GraphPad Prism 9.5.0. **b** Co-IP showed that the binding of VASH2 to α-tubulin in H460 cells was enhanced by KY216 (20 nM) (independant

biological replicates n = 3). **c** Raw data and binding isotherms from ITC measurements of KY216 binding to tubulin. The data shown are representative of two independent biological experiments, with mean binding affinity and thermodynamic parameters of the replicates displayed alongside the binding isotherms. **d** ITC results for KY216 and VASH2 interaction, showing no significant change in ΔH, indicating no binding (independant biological replicates n = 3). **e** ITC analysis of VASH2 binding to tubulin. The data shown are representative of three independent biological experiments, with mean binding affinity and thermodynamic parameters of the three replicates displayed alongside the binding isotherms. **f** ITC analysis of VASH2 binding to tubulin in the presence of KY216. The data shown are representative of three independent biological experiments, with mean binding affinity and thermodynamic parameters of the three replicates displayed alongside the binding isotherms. Source data are provided as a Source Data file.

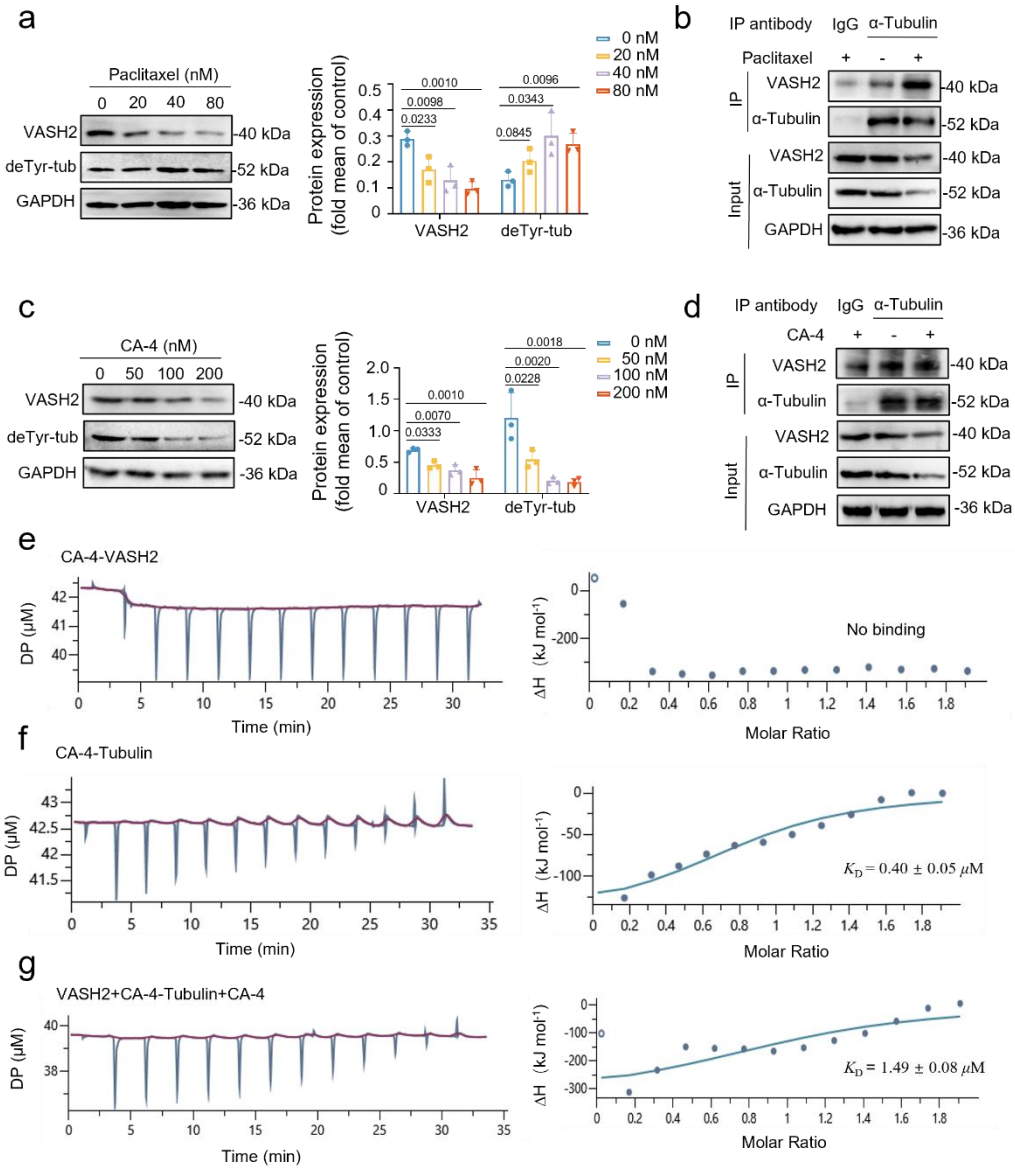

Supplementary Fig. 8. **Effects of paclitaxel and Combretastatin A-4 on VASH2 and microtubule protein de-tyrosination.** **a** Western blot analysis revealed the effects of different concentrations of paclitaxel on VASH2 and detry-tubulin expression in H460 cells (independant biological replicates n = 3). **b** Immunoprecipitation (co-IP) assay was performed to evaluate the potential effect of 40 nM paclitaxel on the interaction of VASH2 with α-tubulin in H460 cells (independant biological replicates n = 3). **c** Western blot analysis was used to detect the effect of different concentrations of Combretastatin A-4 on VASH2 and detry-tubulin expression in H460 cells (independant biological replicates n = 3). **d**

co-IP assay was used to investigate the effect of 100 nM Combretastatin A-4 on the interaction of VASH2 with α-tubulin in H460 cells (independant biological replicates n = 3). **e** ITC results for the interaction between CA-4 and VASH2 (independant biological replicates n = 3). **f** Raw data and binding isotherms from ITC measurements of CA-4 binding to tubulin. The data shown are representative of three independent biological experiments, with mean binding affinity and thermodynamic parameters of the replicates displayed alongside the binding isotherms. **g** ITC analysis of VASH2 binding to tubulin in the presence of CA-4. The data shown are representative of three independent biological experiments, with mean binding affinity and thermodynamic parameters of the three replicates displayed alongside the binding isotherms. All data are shown as means ± SEM. Values shown are *P* values and were calculated using the two-tailed Student's *t* tests (**a**) and one-way ANOVA with Tukey's comparisons test (**c**) in GraphPad Prism 9.5.0. Source data are provided as a Source Data file.

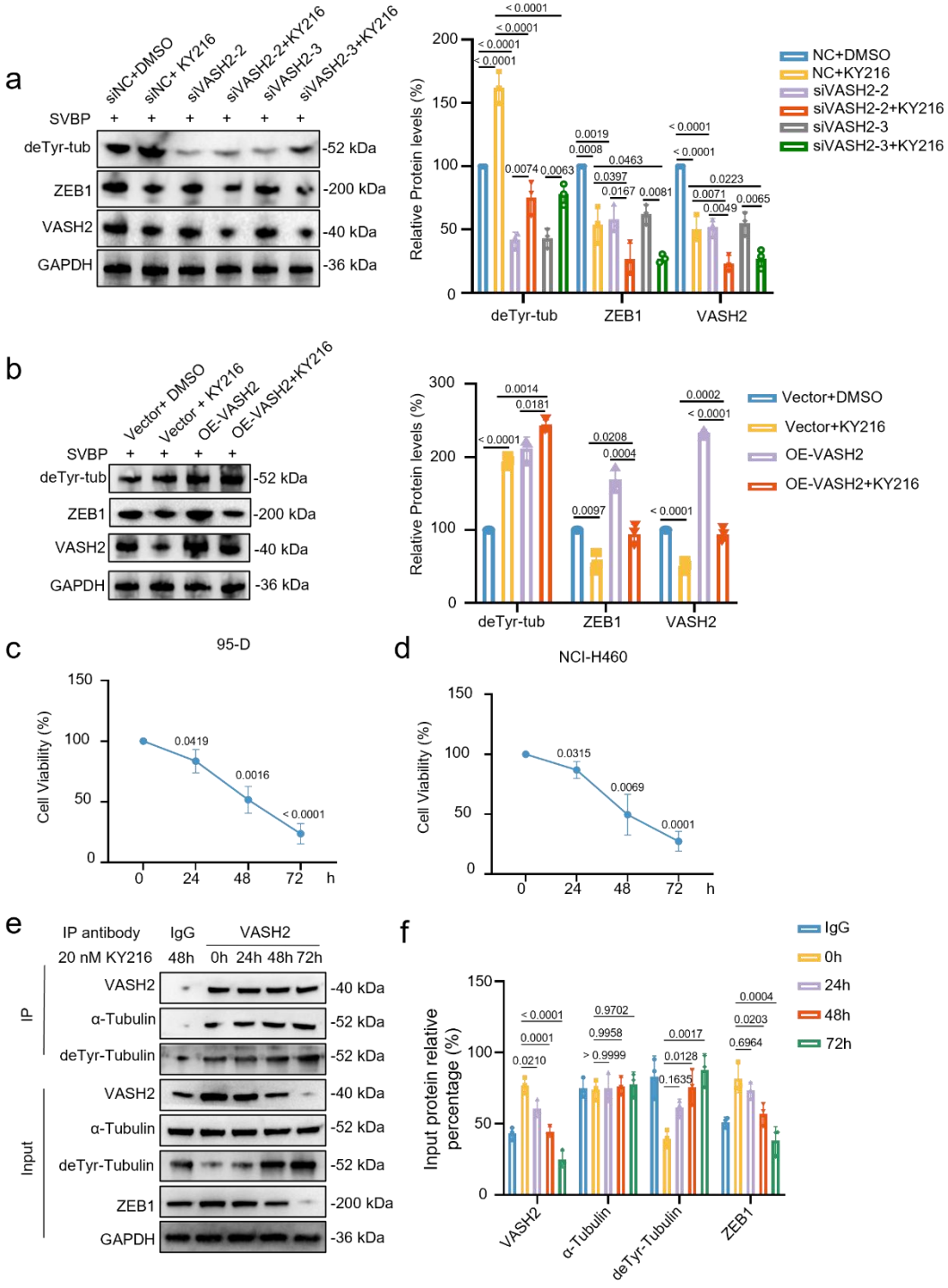

Supplementary Fig. 9. **Effects of KY216 on VASH2-mediated tubulin detyrosination and the EMT process. a** Western blot (left panel) and quantitative analysis (right panel) of deTyr-tub, ZEB1, and VASH2 protein expression in 95-D cells transfected with VASH2 siRNA and treated with 20 nM KY216 (independant biological replicates n = 3). **b** Western blot (left panel) and quantitative analysis (right

panel) of deTyr-tub, ZEB1, and VASH2 protein expression in 95-D cells with VASH2 overexpression and treated with 20 nM KY216 (independant biological replicates n = 3). **c** The CCK-8 assay was used to detect the changes in the viability of 95-D cells treated with KY216 at different time points (0, 24, 48, 72 h) (independant biological replicates n = 3). **d** The CCK-8 assay was used to detect the changes in the viability of NCI-H460 cells treated with KY216 at different time points (0, 24, 48, 72 h) (independant biological replicates n = 3). **e** By means of Co-IP and the corresponding Input samples, the level changes of VASH2, detry-tub, ZEB1, and α-tubulin after KY216 treatment at different time points were detected. Among them, the Input samples reflect the expression status of endogenous proteins in the cells (independant biological replicates n = 3). **f** Quantitative analysis of the proportion of each protein in the input samples in subfigure **e** (independant biological replicates n = 3). All data are shown as means ± SEM. Values shown are *P* values and were calculated using the one-way ANOVA with Tukey's comparisons test in GraphPad Prism 9.5.0. Source data are provided as a Source Data file.

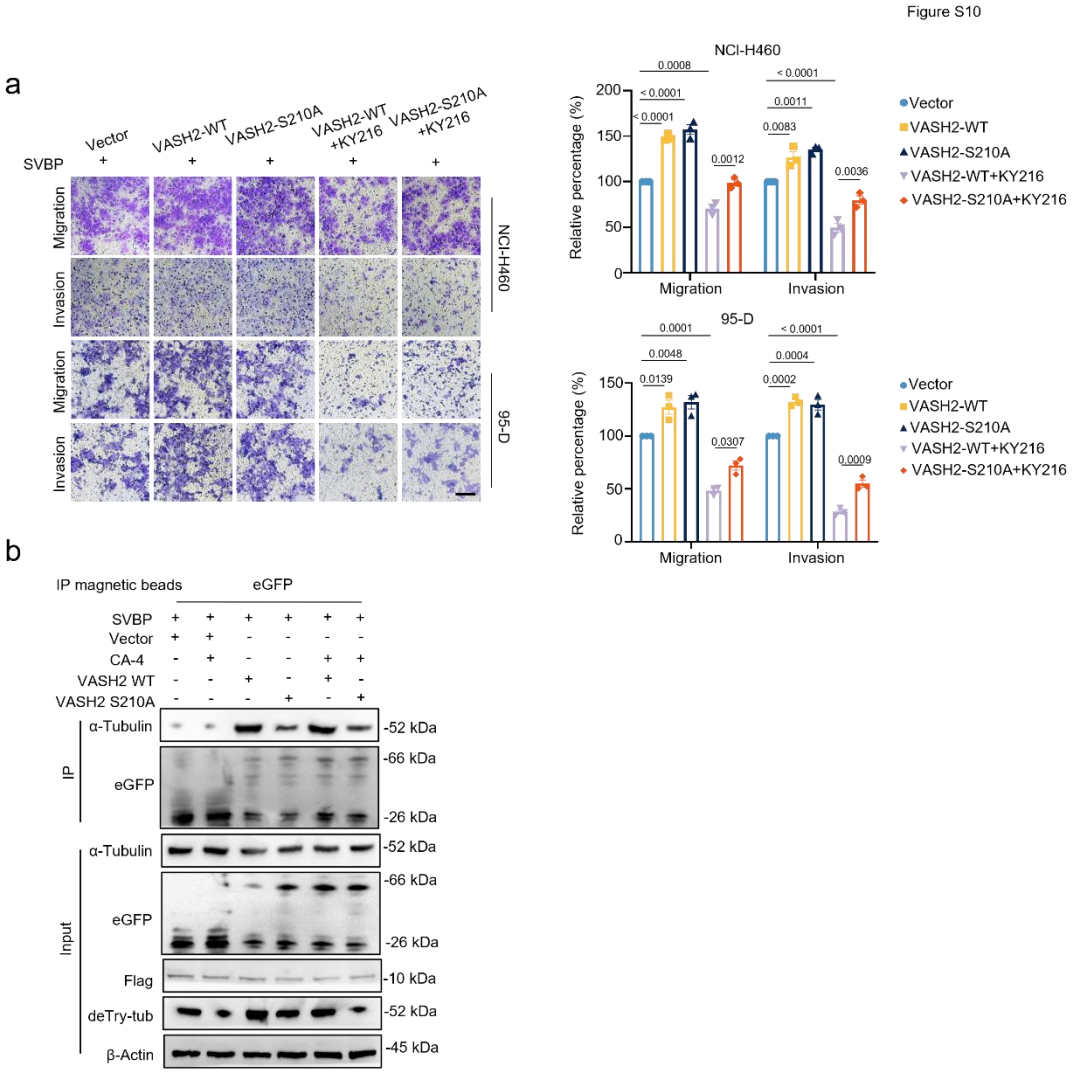

Supplementary Fig. 10. **The effect of VASH2-S210 mutation on the actions of KY216 and CA-4.** **a** Transwell assays was utilized to detect the migration and invasion of NCI-H460 and 95-D cells following transfection of VASH2-WT and VASH2-S210A mutant plasmids in the presence of KY216 (independant biological replicates n = 3). **b** Co-IP assay was used to study changes in the interaction between VASH2 (eGFP-tagged) and α-tubulin after transfection of VASH2-WT and VASH2-S210A mutant plasmids in the presence of CA-4 in 95-D cells (independant biological replicates n = 3). All data are shown as means ± SEM. Values shown are *P* values and were calculated using the one-way ANOVA with Tukey's comparisons test in GraphPad Prism 9.5.0. Source data are provided as a Source Data file.

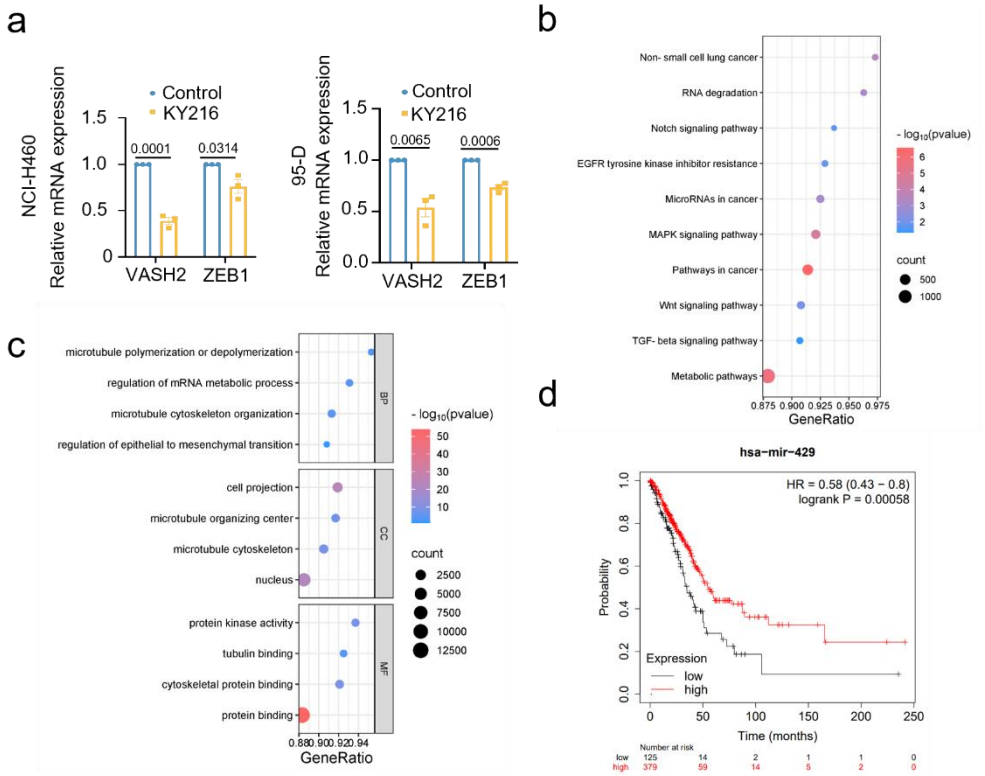

Supplementary Fig. 11. **Effects of miR-429 on migration and invasion of NSCLC.** **a** The levels of VASH2 and ZEB1 gene in the presence of KY216 in 7×10^5 NCI-H460 and 95-D cells were tested by qRT-PCR (independant biological replicates n = 3). All data are shown as means ± SEM. Values shown are *P* values and were calculated using a two-tailed Student's *t* tests in GraphPad Prism 9.5.0. **b** KEGG enrichment analysis of cellular pathways potentially targeted by differentially expressed miRNAs following KY216 treatment. **c** GO enrichment analysis of biological processes potentially associated with differentially expressed miRNAs post KY216 treatment. **d** The overall survival of miR-429 in pan-cancer analyzed by the Kaplan-Meier Plotter database, revealed that high expression of miR-429 was associated with longer survival in lung cancer patients. Source data are provided as a Source Data file.

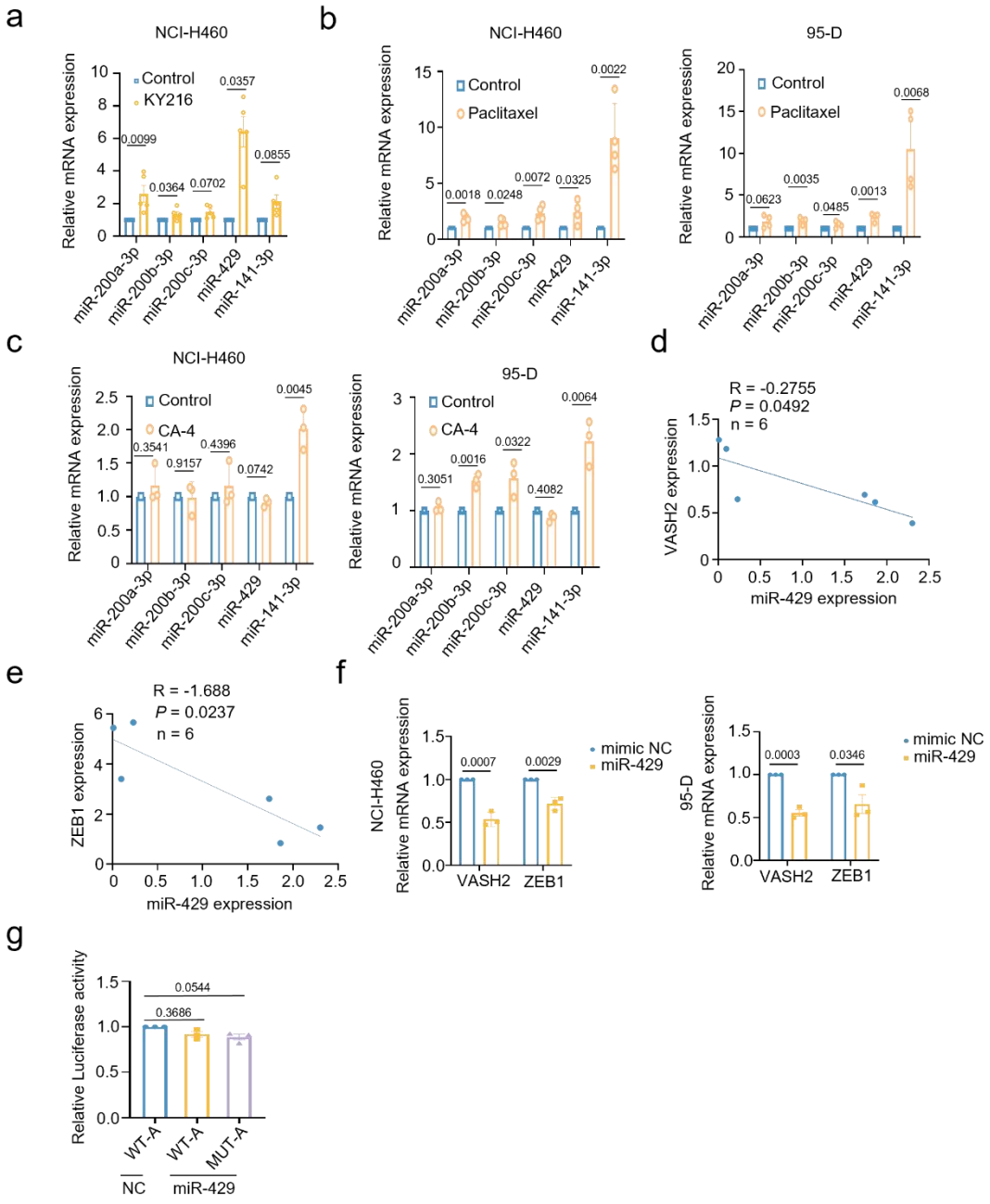

Supplementary Fig. 12. **The correlation between miR-429 and VASH2. a** Detection of gene level changes in miR-200 family after KY216 treatment was performed using qRT-PCR (independant biological replicates n = 5). **b** qRT-PCR assay assessing the expression of the miR-200 family genes in NSCLC cells treated with 40 nM paclitaxel for 48 hours (independant biological replicates n = 3). **c** Assessment of miR-200 family gene expression levels in NSCLC cells following treatment with 100 nM Combretastatin A-4 for 48 hours, utilizing qRT-PCR (independant biological

replicates n = 3). **d, e** Correlation analysis reveals the relationship between the expression of miR-429 and the mRNA expression of VASH2 and ZEB1 before and after KY216 treatment (independant biological replicates n = 6). Pearson's correlation coefficient was used for linear-correlation analysis. **f** The qRT-PCR analysis demonstrated that the overexpression of miR-429 resulted in decreased gene expression of VASH2 and ZEB1 in both cell lines (independant biological replicates n = 3). **g** 293T cells were co-transfected with NC, miR-429, pmiR-GLO-VASH2-WT-A, and pmiR-GLO-VASH2-Mut-A, the value of firefly luciferase (F-luc) was normalized to that of the renilla luciferase (R-luc) (independant biological replicates n = 3), ns indicates no significant difference. All data are shown as means ± SEM. Values shown are *P* values and were calculated using the two-tailed Student's *t* tests (**a-f**) and one-way ANOVA with Tukey's comparisons test (**g**). Source data are provided as a Source Data file.

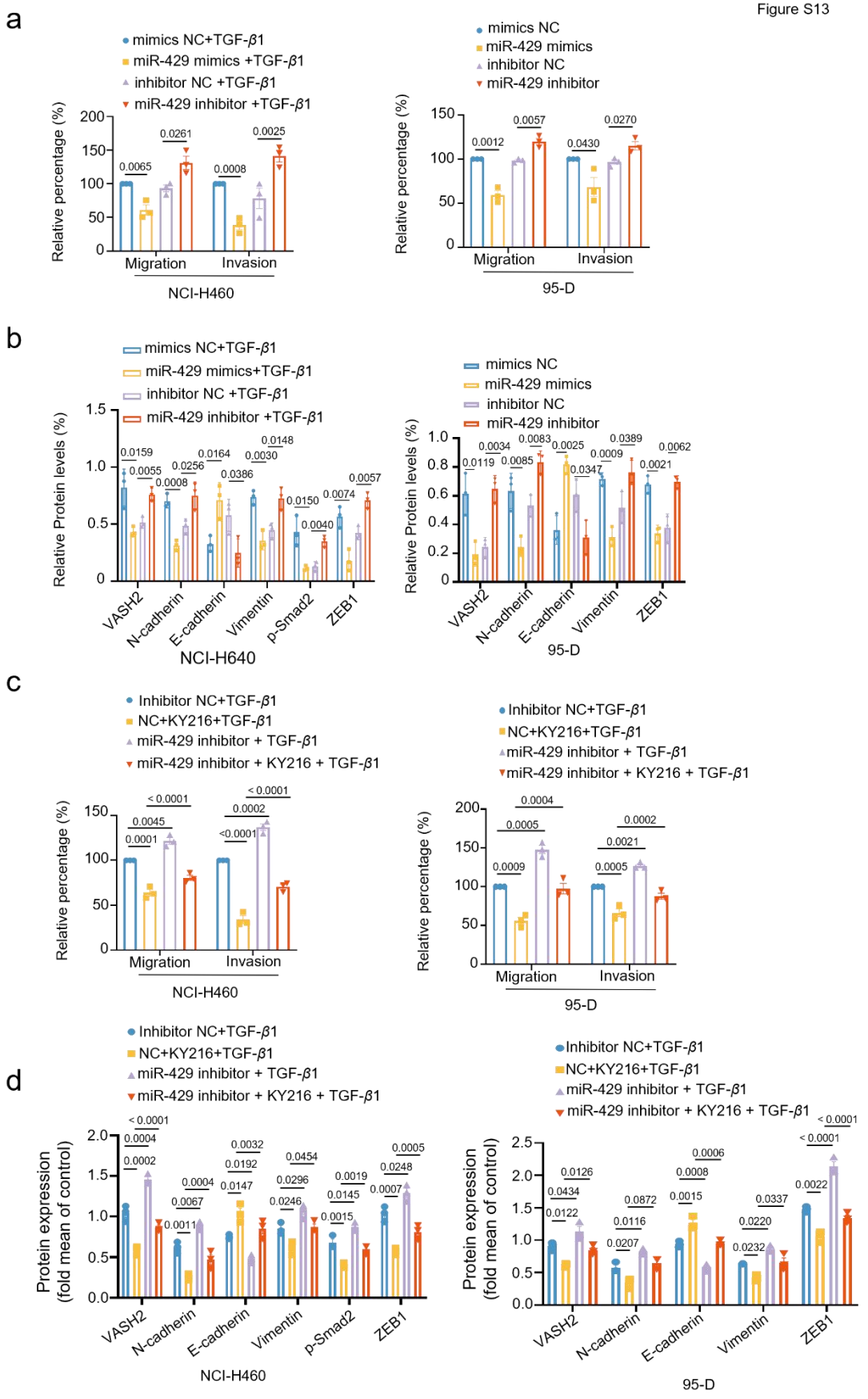

Supplementary Fig. 13. **Effects of miR-429 on migration and invasion of NSCLC.**

a Quantitative data on the effects of miR-429 mimics and miR-429 inhibitor on the migration and invasion of NCI-H460 and 95-D cells (independant biological replicates n = 3). **b** Quantitative data on the effects of miR-429 mimics and miR-429 inhibitor on the expression of epithelial/mesenchymal markers, p-Smad2, and ZEB1 protein in NCI-H460 and 95-D cells (independant biological replicates n = 3). **c** Quantitative data demonstrating that overexpression of miR-429 counteracts the inhibitory effect of KY216 on migration and invasion of TGF-*β*-induced NCI-H460 and 95-D cells (independant biological replicates n = 3). **d** Quantitative data demonstrating that overexpression of miR-429 counteracts the inhibitory effect of KY216 on epithelial/mesenchymal markers, p-Smad2 and ZEB1 (independant biological replicates n = 3). All data are shown as means ± SEM. Values shown are *P* values and were calculated using the two-tailed Student's *t* tests (**a, b**) and one-way ANOVA with Tukey's comparisons test (**c, d**). Source data are provided as a Source Data file.

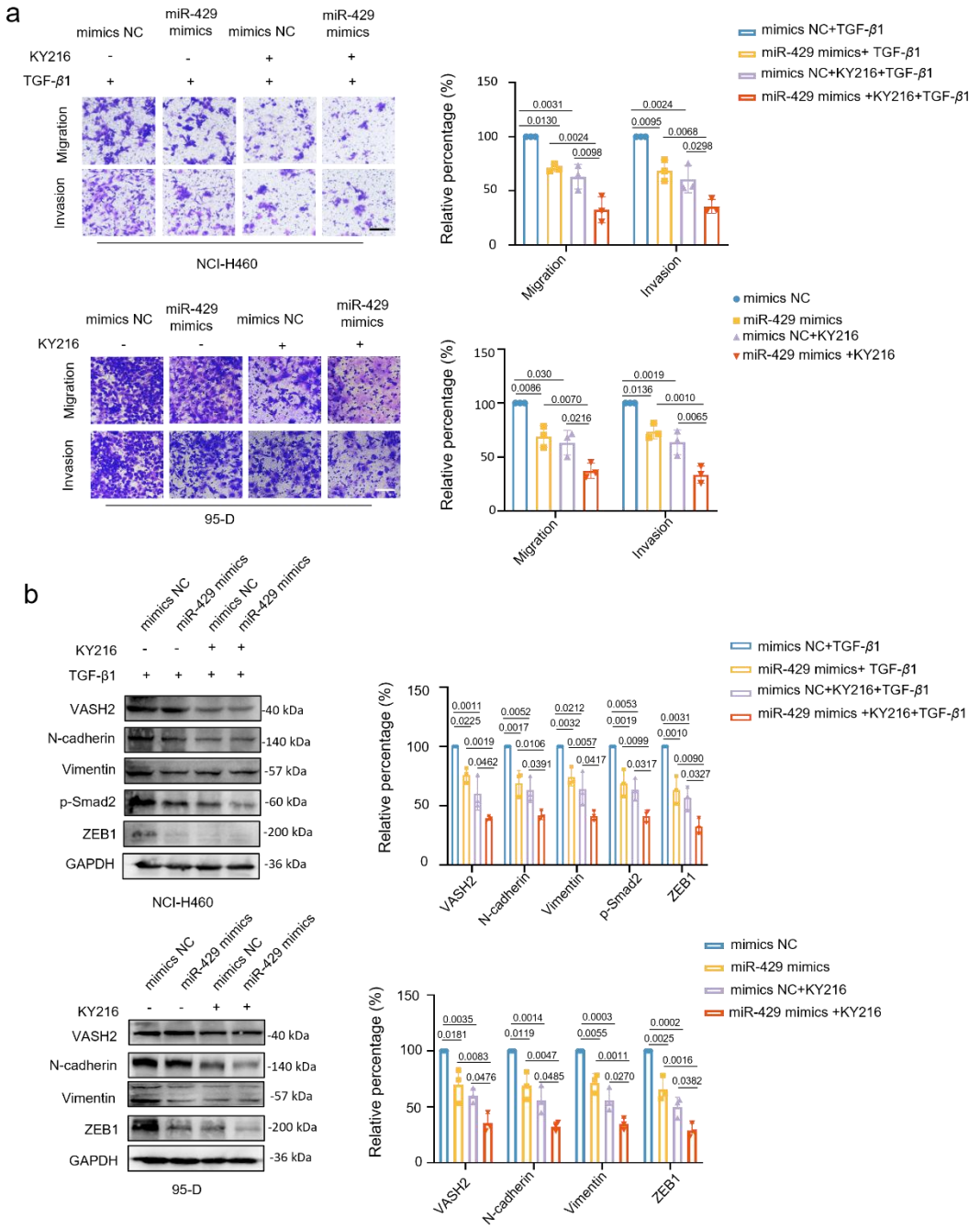

Supplementary Fig. 14. **Transfection of miR-429 mimics enhanced the inhibitory effect of KY216 on migration and invasion.** **a** Representative image of trans-well assay of NCI-H460 and 95-D cells treated with different treatments and their quantitatively analyzed cell migration numbers are shown (independant biological replicates n = 3). Scale bar: 50 μm. **b** Representative Western blot analysis and corresponding quantitative analysis of epithelial and mesenchymal markers, as well as

ZEB1 protein expression, are shown (independant biological replicates n = 3). All data are shown as means ± SEM. Values shown are *P* values and were calculated using the one-way ANOVA with Tukey's comparisons test in GraphPad Prism 9.5.0. Source data are provided as a Source Data file.

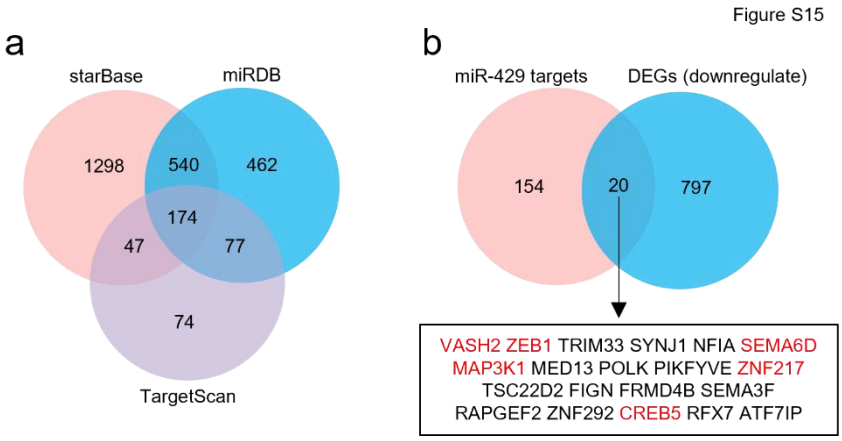

Supplementary Fig. 15. **The KY216/miR-429 regulatory network identified through bioinformatics analysis screening.** **a** A Venn diagram illustrating the intersection analysis of miR-429 potential target genes predicted by the starBase, miRDB, and TargetScan databases. **b** A Venn diagram showing the intersection analysis of miR-429 candidate target genes and downregulated genes after KY216 treatment.

Figure S16

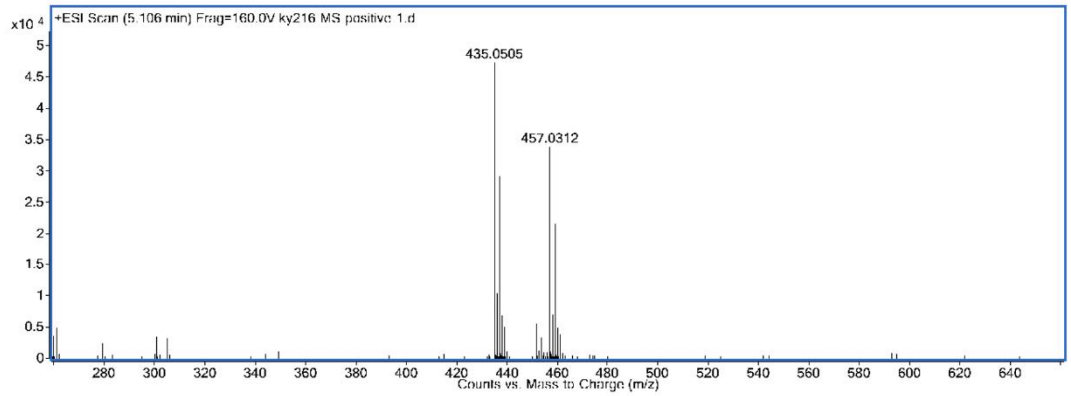

Elemental Composition Calculator

Target m/z:	435.0505	**Result type:**	Positive ions	**Species:**	$[M+H]^+$
Ion Formula		**Calculated m/z**		**PPM Error**	
C20H17Cl2N2O5		435.0509		0.97	

Supplementary Fig. 16. **High-resolution ESI-MS (positive mode) of KY216 displayed a protonated molecule $[M+H]^+$ at m/z435.0505, corresponding to the elemental composition of $C_{20}H_{17}Cl_2N_2O_5$.**

Figure S17

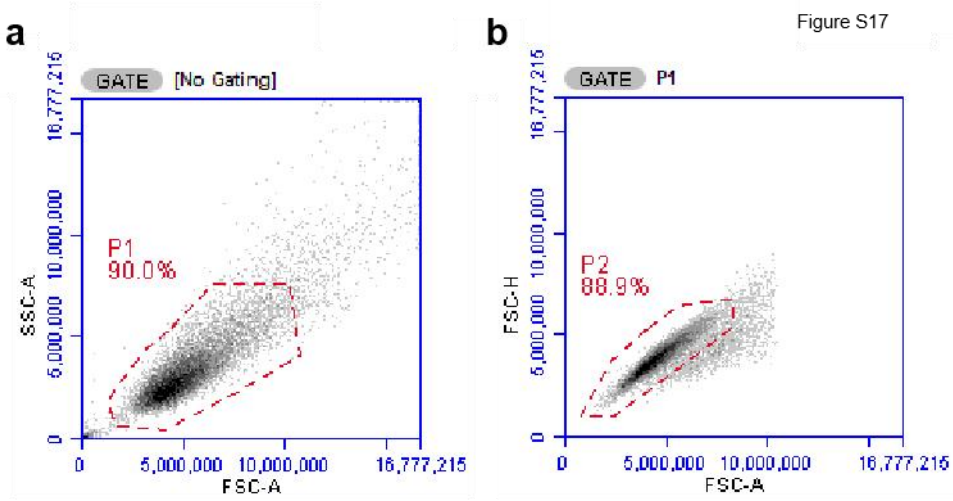

Supplementary Fig. 17. **Gating strategy for flow cytometric cell cycle analysis.** **a** Initial gating (P1) was set on the forward scatter-area (FSC-A) vs. side scatter-area (SSC-A) dot plot to identify the main population of intact cells and exclude debris and aggregates. 90.0% of the total events fell within this gate. **b**

Subsequent gating (P2) was applied to the P1-gated population using FSC-height (FSC-H) vs. FSC-A to exclude doublets or cell aggregates, ensuring the analysis of single cells. 88.9% of the events from the P1 gate were identified as singlets within the P2 gate. This gating strategy was consistently applied to all flow cytometric cell cycle analyses throughout this study.

Supplemental Tables

Supplementary Table 1. Summary table of binding parameters for each pair, including binding affinity (K_D ± SD), enthalpy change (ΔH ± SD), Gibbs free energy change (ΔG ± SD), entropy change (-TΔS ± SD), and binding site number (N ± SD).

Protein (Syringe)	Protein (Cell)	K_D (μM) (mean ± SD)	ΔH ± SD (kJ mol^{-1})	ΔG ± SD (kJ mol^{-1})	-TΔS ± SD (kJ mol^{-1})	N ± SD (sites)	Replicates
KY216	Tubulin	0.15 ± 0.01	-86.35 ± 26.38	-39.4 ± 0.14	47.1 ± 26.3	0.83 ± 0.09	2
CA-4	Tubulin	0.40 ± 0.05	-161.0 ± 23.64	-36.57 ± 0.38	124.3 ± 23.18	1.08 ± 0.20	3
VASH2	Tubulin	1.53 ± 0.22	-321.3 ± 23.67	-33.27 ± 0.35	288.3 ± 23.67	1.02 ± 0.23	3
VASH2 + KY216	Tubulin + KY216	0.52 ± 0.10	-180.0 ± 24.06	-35.97 ± 0.50	143.7 ± 24.11	1.11 ± 0.22	3
VASH2 + CA-4	Tubulin + CA-4	1.49 ± 0.08	-338.0 ± 3.61	-33.3 ± 0.10	305.0 ± 3.61	1.44 ± 0.26	3

Supplementary Table 2. Standard peak listings for 1H NMR and proton-decoupled 13C NMR for all compounds.

Compound	Analytical Data
(S)-2-((tert-butoxycarbonyl)amino)-3-(2,3-dihydrobenzo-[b][1,4]dioxin-6-yl)propanoate (**2**)	1H NMR (600 MHz, Chloroform-d) δ 6.75 (d, J = 8.2 Hz, 1H), 6.61 (s, 1H), 6.56 (d, J = 8.1 Hz, 1H), 5.28 (s, 1H), 4.99 (d, J = 7.8Hz, 1H), 4.51 (q, J = 5.9 Hz, 1H), 4.21 (s, 4H), 3.71 (s, 3H), 2.98(dd, J = 13.8, 5.4 Hz, 1H), 2.93 (dd, J = 13.9, 5.9 Hz, 1H), 1.41 (s,9H).
(S)-5-((2,3-Dihydrobenzo[b][1,4]dioxin-6-yl)methyl)-imidazolidine-2,4-dione (**3**).	1H NMR (600 MHz, MeOD) δ 6.74 (d, J = 8.2 Hz, 1H), 6.72 (d, J = 1.8 Hz, 1H), 6.67 (dd, J = 8.2, 1.9 Hz, 1H), 4.32 (t, J = 5.1 Hz, 1H), 4.20 (s, 4H), 2.98 (dd, J = 14.2, 4.5 Hz, 1H), 2.91 (dd, J = 14.2, 5.6 Hz, 1H).
(6R,10aS)-6-(3,5-Dichloro-4-methoxyphenyl)-2,3,10a,11-tetrahydro-[1,4]dioxino[2,3-g]imidazo[1,5-b]isoquinoline-8,10(6H,9H)-dione (**KY216**)	m.p. 249.6−250.3 °C; 1H NMR (500 MHz, Chloroform-d) δ 7.75 (s, 1H), 7.19 (s, 2H), 6.76 (s, 1H), 6.44 (s, 1H), 5.98 (s, 1H), 4.26 (d, J = 9.9 Hz, 4H), 4.18 (dd, J = 11.7, 5.1Hz, 1H), 3.89 (s, 3H), 3.21 (dd, J = 15.8, 5.1 Hz, 1H), 2.90 (dd, J = 15.6, 11.7 Hz, 1H); 13C

	NMR (125 MHz, Chloroform-d) δ 172.78, 154.23, 152.35, 143.66, 143.20, 139.29, 129.93, 128.85, 125.37, 124.43, 117.47, 116.90, 64.54, 64.49, 60.85, 53.90, 53.52, 29.91; HRMS: $[M + H]^+$ calcd for $C_{20}H_{17}Cl_2N_2O_5$, 435.0509, found 435.0505; HPLC purity: 97.684%.

Supplementary Table 3. Human primers for qRT-PCR

Gene	Forward (5' - 3')	Reverse (5' - 3')	Reverse transcription primer [a]
GAPDH	AGATCCCTCCAAAATCAAGTGG	GGCAGAGATGATGACCCTTTT	/
VASH2	GCTGGTCCTCAACGTCTCAA	CTGGGGGACAGGGATTTTCC	/
ZEB1	GATGACCTGCCAACAGACCA	CCCCAGGATTTCTTGCCCTT	/
miR-429	CGCGCGTAATACTGTCTGGTAA	AGTGCAGGGTCCGAGGTATT	GTCGTATCCAGTGCAGGGTCCGAGGTATTCGCACTGGATACGACACGGTT
miR-200a	GCGCGTAACACTGTCTGGTAA	AGTGCAGGGTCCGAGGTATT	GTCGTATCCAGTGCAGGGTCCGAGGTATTCGCACTGGATACGACACATCG
miR-200b	GCGCGTAATACTGCCTGGTAA	AGTGCAGGGTCCGAGGTATT	GTCGTATCCAGTGCAGGGTCCGAGGTATTCGCACTGGATACGACTCATCA
miR-200c	CGCGTAATACTGCCGGGTAAT	AGTGCAGGGTCCGAGGTATT	GTCGTATCCAGTGCAGGGTCCGAGGTAT

			TCGCACTGGATACG ACTCCATC
miR-141	GCGCGTAACAC TGTCTGGTAA	AGTGCAGGGTC CGAGGTATT	GTCGTATCCAGTGC AGGGTCCGAGGTAT TCGCACTGGATACG ACCCATCT

[a] Primers used in stem-loop miRNA cDNA synthesis.

Supplementary Table 4. Patient tissues information

NO.	Sex[a]	Organ	Pathology diagnosis	Type	Lymph node metastasis[b]	Survival (month)	Survive or not[c]
1	Male	Lung	Lung Squamous Cell Carcinoma	Malignant	0	108	0
2	Female	Lung	Lung Squamous Cell Carcinoma	Malignant	1	16	1
3	Male	Lung	Lung Squamous Cell Carcinoma	Malignant	1	86	0
4	Male	Lung	Lung Squamous Cell Carcinoma	Malignant	1	107	0
5	Male	Lung	Lung Squamous Cell Carcinoma	Malignant	0	85	0
6	Male	Lung	Lung Squamous Cell Carcinoma	Malignant	1	79	0
7	Female	Lung	Lung Squamous Cell Carcinoma	Malignant	1	36	1
8	Male	Lung	Lung Squamous Cell Carcinoma	Malignant	0	50	1
9	Male	Lung	Lung Squamous	Malignant	0	105	0

			Cell Carcinoma				
10	Male	Lung	Lung Squamous Cell Carcinoma	Malignant	0	7	0
11	Male	Lung	Lung Squamous Cell Carcinoma	Malignant	1	108	0
12	Male	Lung	Lung Squamous Cell Carcinoma	Malignant	0	44	1
13	Male	Lung	Lung Squamous Cell Carcinoma	Malignant	0	102	0
14	Male	Lung	Lung Squamous Cell Carcinoma	Malignant	1	101	0
15	Male	Lung	Lung Squamous Cell Carcinoma	Malignant	1	16	1
16	Male	Lung	Lung Squamous Cell Carcinoma	Malignant	0	56	1
17	Male	Lung	Lung Squamous Cell Carcinoma	Malignant	1	102	0
18	Male	Lung	Lung Squamous Cell Carcinoma	Malignant	0	81	0
19	Male	Lung	Lung Squamous Cell Carcinoma	Malignant	1	31	1
20	Male	Lung	Lung Squamous Cell Carcinoma	Malignant	0	18	1
21	Male	Lung	Lung Squamous Cell Carcinoma	Malignant	0	102	0
22	Male	Lung	Lung Squamous Cell Carcinoma	Malignant	1	80	1
23	Male	Lung	Lung Squamous Cell Carcinoma	Malignant	0	105	0

24	Female	Lung	Lung Squamous Cell Carcinoma	Malignant	0	28	1
25	Male	Lung	Lung Squamous Cell Carcinoma	Malignant	1	104	0
26	Male	Lung	Lung Squamous Cell Carcinoma	Malignant	0	104	0
27	Male	Lung	Lung Squamous Cell Carcinoma	Malignant	1	92	0
28	Male	Lung	Lung Squamous Cell Carcinoma	Malignant	0	32	1
29	Male	Lung	Lung Squamous Cell Carcinoma	Malignant	0	62	1
30	Male	Lung	Lung Squamous Cell Carcinoma	Malignant	0	31	1
31	Male	Lung	Lung Squamous Cell Carcinoma	Malignant	0	90	0
32	Male	Lung	Lung Squamous Cell Carcinoma	Malignant	1	86	0
33	Female	Lung	Lung Squamous Cell Carcinoma	Malignant	1	55	1
34	Female	Lung	Lung Squamous Cell Carcinoma	Malignant	1	104	0
35	Male	Lung	Lung Squamous Cell Carcinoma	Malignant	0	90	0
36	Male	Lung	Lung Squamous Cell Carcinoma	Malignant	0	106	0
37	Male	Lung	Lung Squamous Cell Carcinoma	Malignant	1	82	0
38	Male	Lung	Lung	Malignant	0	67	0

			adenocarcinoma				
39	Male	Lung	Lung adenocarcinoma	Malignant	0	52	0
40	Female	Lung	Lung adenocarcinoma	Malignant	1	66	0
41	Female	Lung	Lung adenocarcinoma	Malignant	1	29	1
42	Male	Lung	Lung adenocarcinoma	Malignant	0	9	1
43	Female	Lung	Lung adenocarcinoma	Malignant	0	16	1
44	Female	Lung	Lung adenocarcinoma	Malignant	0	63	0
45	Female	Lung	Lung adenocarcinoma	Malignant	1	39	1
46	Female	Lung	Lung adenocarcinoma	Malignant	0	50	1
47	Female	Lung	Lung adenocarcinoma	Malignant	1	8	1
48	Male	Lung	Lung adenocarcinoma	Malignant	0	50	1
49	Female	Lung	Lung adenocarcinoma	Malignant	0	49	0
50	Male	Lung	Lung adenocarcinoma	Malignant	0	43	1
51	Female	Lung	Lung adenocarcinoma	Malignant	1	43	0
52	Female	Lung	Lung adenocarcinoma	Malignant	1	58	0

53	Male	Lung	Lung adenocarcinoma	Malignant	1	4	1
54	Female	Lung	Lung adenocarcinoma	Malignant	1	59	0
55	Male	Lung	Lung adenocarcinoma	Malignant	0	25	1
56	Female	Lung	Lung adenocarcinoma	Malignant	0	44	1
57	Male	Lung	Lung adenocarcinoma	Malignant	0	40	1
58	Female	Lung	Lung adenocarcinoma	Malignant	0	72	0
59	Male	Lung	Lung adenocarcinoma	Malignant	0	77	0
60	Male	Lung	Lung adenocarcinoma	Malignant	1	68	0
61	Male	Lung	Lung adenocarcinoma	Malignant	0	48	1
62	Male	Lung	Lung adenocarcinoma	Malignant	1	59	0
63	Female	Lung	Lung adenocarcinoma	Malignant	0	69	0
64	Female	Lung	Lung adenocarcinoma	Malignant	1	37	1
65	Female	Lung	Lung adenocarcinoma	Malignant	0	17	1
66	Male	Lung	Lung adenocarcinoma	Malignant	1	24	1
67	Female	Lung	Lung	Malignant	1	48	0

			adenocarcinoma				
68	Male	Lung	Lung adenocarcinoma	Malignant	1	49	0
69	Female	Lung	Lung adenocarcinoma	Malignant	1	31	1
70	Female	Lung	Lung adenocarcinoma	Malignant	1	44	1
71	Male	Lung	Lung adenocarcinoma	Malignant	1	16	1
72	Male	Lung	Lung adenocarcinoma	Malignant	0	45	0
73	Female	Lung	Lung adenocarcinoma	Malignant	0	68	0
74	Female	Lung	Lung adenocarcinoma	Malignant	1	21	1
75	Female	Lung	Lung adenocarcinoma	Malignant	0	16	1

[a] The sex of the participants is classified based on biological characteristics such as chromosomes, sexual organs, and endogenous hormone levels.

[b] 1 indicates the presence of lymph node metastasis and 0 indicates the absence of lymph node metastasis.

[c] death = 1 / live = 0.